

00

# The influence of the longitudinal magnetic field on the polarization of the photon echo and the stimulated photon echo formed in a gas at $0 \leftrightarrow 1$ transition

© N.N. Rubtsova<sup>1</sup>, S.A. Kochubei<sup>1</sup>, E.B. Khvorostov<sup>1</sup>, V.A. Reshetov<sup>2</sup>

<sup>1</sup>Rzhanov Institute of Semiconductor Physics, Siberian Branch, Russian Academy of Sciences, Novosibirsk, Russia

<sup>2</sup>Togliatti State University, Togliatti, Russia

e-mail: eugeny@isp.nsc.ru

Received March 19, 2023

Revised May 07, 2024

Accepted April 01, 2024

A review of the methods of theoretical and experimental studies of the polarization of photon echo and stimulated photonic echo formed at the  $0 \leftrightarrow 1$  transition of  $^{174}\text{Yb}$  atoms, depending on the strength of the longitudinal magnetic field, is performed. The non-Faraday rotation of the polarization plane of the photon echo in the limit of a weak magnetic field and the „unpolarized“ echo in the limit of a strong magnetic field are discussed.

**Keywords:** photon echo, stimulated photon echo, non-Faraday rotation of the polarization plane of the photon echo in a magnetic field.

DOI: 10.61011/EOS.2024.05.59116.5569-24

## 1. Introduction

Photon echo and its modifications are used not only to study relaxation processes in various media (in case of gases — to study collisions), but also in data recording, processing and reproduction of information. In this context, a stimulated photon echo phenomena is of most importance [1–3]. Photon echo signals may be quite intensive and comparable with excitation pulse power [4]. Therefore, it is interesting to study the effect of external fields on echo response parameters.

This overview describes the methods used to investigate the effect of a longitudinal magnetic field on photon echo (PE) and stimulated photon echo (SPE) signals in gas at the  $0 \leftrightarrow 1$  transition, and results of research.

## 2. Photon echo generated in gas at the $0 \leftrightarrow 1$ transition in a longitudinal magnetic field

### 2.1. On the nature of magnetic rotation of PE polarization

Recall that PE is coherent radiation emitted by a medium after the end of exposure to a series of intensive short pulses from a resonance electromagnetic (light) field and caused by phase re-matching between individual emitters [5–8]. In this case we deal with two pulses of radiation resonant to the  $J = 1 \leftrightarrow J = 0$  transition that are separated by the delay time  $\tau$  with durations  $T_1$  and  $T_2$ . On the assumption that  $\tau \gg T_i$  ( $i = 1, 2$ ), the coherent echo response is generated approximately at  $t \approx 2\tau$  after arrival of the first excitation pulse. The optically allowed transition  $J = 1 \leftrightarrow J = 0$  is

the most simple one, for which the non-Faraday rotation of polarization plane exists as predicted in [9].

In the general case of optical transition in an atom or molecule with arbitrary angular momenta of the upper active level  $J_a$  and lower active level  $J_b$ , the PE polarization in a zero magnetic field is defined by many factors. These are primarily the type of transition and particular angular momenta of the active levels. Another factor is the polarization of excitation radiation pulses. The excitation pulse areas defined as  $\theta_i \approx \frac{de_i T_i}{\hbar}$  ( $d$  is the matrix element of the transition dipole moment,  $e_i$  is the electric field of the  $i$ th pulse,  $T_i$  is its width) can also affect the PE response polarization. Finally, the PE polarization may vary when subjected to depolarizing collision anisotropy.

In a particular case of the  $0 \leftrightarrow 1$  optical transition, the PE polarization (without a magnetic field) does not depend on the excitation pulse areas of resonance radiation [10]. The effect of depolarizing collisions may be neglected in the experiment conditions described below. Therefore, the polarization of PE generated at the  $0 \leftrightarrow 1$  transition with the zero magnetic field is only defined by the level structure and excitation pulse polarization.

The nature of the non-Faraday rotation of the PE polarization plane in gas at the  $0 \leftrightarrow 1$  transition may be explained as follows. We assume that both wave vectors  $\mathbf{k}_i$  of the resonance radiation excitation pulses are parallel to  $Oz$  as shown in Figure 1. The longitudinal magnetic field is also oriented along the  $Oz$  axis coinciding with the axis of symmetry of the gas cell. We also take the  $Oz$  axis as the quantization axis; in such experimental geometry, right-/left-hand-polarized waves propagating along  $Oz$  will be the eigen states of polarization. Without a magnetic field, the upper active level is triply degenerate; the electric

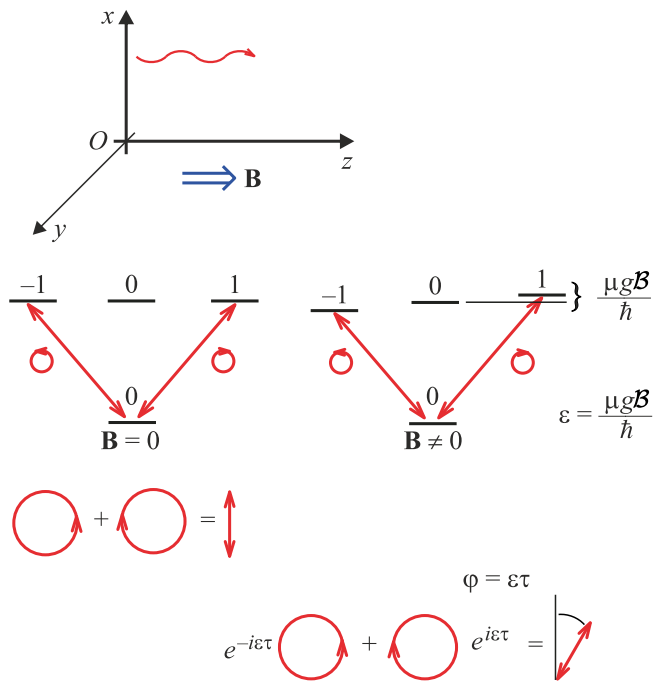


**Figure 1.** Diagram of formation of the PE polarization rotation in gas at the  $0 \leftrightarrow 1$  transition in a weak longitudinal magnetic field.

field vectors of the radiation excitation pulses oscillate in the  $xOy$  plane. In the next experiments, either both electric field vectors are parallel to the  $Ox$  axis or the electric field of the second pulse is parallel to the  $Oy$  axis (cross polarizations of excitation pulses). The excitation radiation linearly polarized along the  $Ox$  axis may be represented as a sum of right-hand and left-hand polarized circular components. These two components create optical coherences at the  $M = 0 \leftrightarrow M = -1$  and  $M = 0 \leftrightarrow M = +1$  transitions. After the end of the first excitation pulse, both optical coherences start oscillating at the frequency  $\omega_{ab} + kv_z$  — this is a polarization decay process due to the Doppler effect (free polarization decay), i.e. excited particle dephasing. Depending on the spectral width and intensity of the first excitation pulse, this may be a set of particles within the total Doppler profile or groups of particles in a range of longitudinal velocity values  $v_z$ . The second excitation radiation pulse of the same polarization as the first one can compensate this dephasing (perform phase reversal), thus by the time of the pulse end the phase difference  $kv_z\tau$  acquired during the delay between pulses  $\tau$  transforms into  $-kv_z\tau$ ; therefore, the initial phased state of optical coherences can be restored by the end of the second time interval  $\tau$  after the second excitation pulse. Consequently, the PE signal is generated at  $t \approx 2\tau$  after arrival of the first excitation pulse. The phase  $e^{i\omega_{ab}\tau}$  that is common for both specified optical transitions does not appear eventually (in the PE polarization).

In a weak longitudinal magnetic field, the upper level with  $J = 1$  is split by  $\frac{2\mu g \mathcal{B}}{\hbar}$  due to the Zeeman effect, where

$\mu$  is the Bohr magneton,  $g$  is the upper level g-factor,  $\mathcal{B}$  is the magnetic field strength. In this case the phrase „weak magnetic field“ means that the Zeeman splitting is low compared with the spectral width of the excitation pulses  $1/T_i$ , therefore both transitions are excited symmetrically with the same amplitude. In the presence of the weak longitudinal magnetic field, microscopic polarizations oscillate at their frequencies  $\omega_{ab} - \frac{\mu g \mathcal{B}}{\hbar} + kv_z$  and  $\omega_{ab} + \frac{\mu g \mathcal{B}}{\hbar} + kv_z$ , the phase difference between the right-hand and left-hand polarized circular components achieved during the time interval  $\tau$  is non-zero and shall be considered during phased state restoration. This results in the linear PE polarization rotated at  $\phi = \frac{\mu g \mathcal{B} \tau}{\hbar}$ .

This simplified pattern also makes it possible to anticipate deviations from the linear PE polarization in the longitudinal magnetic field. Excitation radiation frequency offset from the Doppler profile center of the optical transition shall lead to dissimilar excitation amplitudes of the abovementioned  $M = 0 \leftrightarrow M = -1$  and  $M = 0 \leftrightarrow M = +1$  transitions therefore circular polarization shall be added to the linear PE polarization, which shall be recorded as the ellipticity of the PE signal polarization. As the Zeeman splitting increases (while approaching the spectral width of the excitation pulses) and in the limiting case of the „strong“ magnetic field, carrier frequency instability of the excitation radiation may become increasingly evident. Spatial inhomogeneity of the magnetic field in longitudinal or radial directions may obviously also result in distortion of the PE polarization recorded from the total cylindrical cell volume. The effect of the excitation radiation pulse width is not so evident when  $T_i \ll \tau$  is not satisfied; this is the effect that occurred to be the most evident and it is considered in the numerical calculation [13] in this study.

The described phenomenon is known as the non-Faraday rotation of the PE polarization plane in a longitudinal magnetic field. Rotation angle does not depend on the absorbance of the given gas (as opposed to the Faraday effect) and depends on the magnetic field strength, g-factor and delay time between the excitation pulses. After prediction of this phenomenon [9] for the  $0 \leftrightarrow 1$  transition, the non-Faraday rotation of the PE polarization was analyzed for high angular momenta  $J \gg 1$ , small excitation pulse areas and close g-factor values of the active level of the optical transition [11]. Finally, the theoretical analysis was performed for arbitrary areas and arbitrary shape of excitation pulses, arbitrary optical transitions and unequal g-factors of the active levels [12] with a single restriction on the excitation pulse width:  $T_i \ll \tau$ . The findings in [12] imply that PE power oscillations shall be observed for all types of optical transitions, except  $1/2 \leftrightarrow 1/2$ , when the longitudinal magnetic field strength increases. These oscillations are the most contrast (from the maximum PE power to zero) just for  $J = 1 \leftrightarrow J = 0$ . The photon echo formed in gas at the  $J = 1 \leftrightarrow J = 0$  transition by two pulses of linear polarization oriented parallel to the  $Ox$  axis has the following electric field

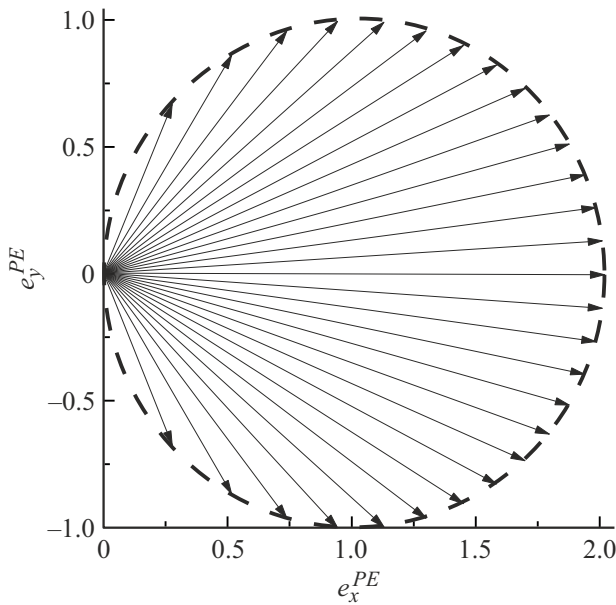


**Figure 2.** Evolution of the PE electric field vector in gas at the  $0 \leftrightarrow 1$  transition in a weak longitudinal magnetic field. When PE is generated by the resonance radiation pulses with the same linear polarization oriented parallel to the  $Ox$  axis, then the PE electric field vector in the zero magnetic field has the maximum length ( $e_x^{PE} = 2$  and  $e_y^{PE} = 0$ ); as the magnetic field increases, the PE electric field vector rotates counterclockwise in the upper half-plane limited by the straight line  $e_y^{PE} = 0$ , and the end of the vector moves on the upper semicircle shown dashed. Point in the origin of coordinates corresponds to „deactivation“ of the PE signal by the weak magnetic field. Further growth of the magnetic field strength is followed by rotation of the PE electric field in the lower half-plane limited by the straight line  $e_y^{PE} = 0$ . If PE is generated by the resonance radiation pulses with linear cross polarizations, then evolution of the PE electric field vector starts from the origin of coordinates and the end of the vector circumscribes the same circle as the magnetic field strength grows.

components (in the specified short pulse approximation).

$$e_x^{PE} = \frac{1}{9}(1 + \cos 2\varepsilon_a \tau), \quad (1)$$

$$e_y^{PE} = \frac{1}{9} \sin 2\varepsilon_a \tau, \quad (2)$$

where  $\varepsilon_a = \mu g_a \mathcal{B} / \hbar$ ,  $g_a = 1.5$  is the  $g$ -factor of the upper active transition level. Possible electric field values of the photon echo with  $e_x^{PE}$  and  $e_y^{PE}$  (in arbitrary units) in the weak longitudinal magnetic field are illustrated in Figure 2.

When looking toward the PE signal propagating along the cell, the picture is as follows. When PE is generated by the resonance radiation pulses with the same linear polarization oriented parallel to the  $Ox$  axis, then the PE electric field vector in the zero magnetic field has the maximum length with  $e_x^{PE} = 2$  and  $e_y^{PE} = 0$ . As the magnetic field grows, the PE electric field vector rotates counterclockwise in the upper half-plane limited by  $e_y^{PE} = 0$ , the end of the PE field

vector moves along the circle shown dashed (whereas  $e_x^{PE}$  first decreases to zero and  $e_y^{PE}$  changes from zero to the maximum value and then back to zero). Point in the origin of coordinates in Figure 2 corresponds to „deactivation“ of the PE signal by the weak magnetic field. Further growth of the magnetic field strength is followed by rotation of the PE electric field vector in the lower half-plane limited by  $e_y^{PE} = 0$ ; whereas  $e_x^{PE}$  grows from zero to the maximum value and  $e_y^{PE}$  changes from zero to the maximum negative value and then back to zero. When PE is generated by the resonance radiation pulses with linear cross polarizations, then evolution of the PE electric field vector starts from the origin of coordinates (for the  $0 \leftrightarrow 1$  transition, there is no PE in such excitation conditions, if collisions may be neglected), the end of the PE electric field vector moves counterclockwise as the magnetic field strength grows, and the end circumscribes the same circle as shown in Figure 2.

The recorded experimental powers of the PE polarization components  $P_x^{PE}$  and  $P_y^{PE}$  obey the following laws:

$$P_x^{PE} \propto (e_x^{PE})^2 \propto \cos^4 \varepsilon_a \tau, \quad (3)$$

$$P_y^{PE} \propto (e_y^{PE})^2 \propto \sin^2 2\varepsilon_a \tau. \quad (4)$$

Oscillations from the maximum value to zero shall be observed for both PE components, while the  $y$ -component oscillates on a twice as high frequency as the  $x$ -component.

Experimental studies known at the time of this writing [13] are represented by the results obtained in Cs atomic vapor [14] (in this case the angular momentum of the lower operating level  $J_b = 3$  or  $J_b = 4$ , and the upper active level with angular momenta  $J_a = 3$  and  $J_a = 4$  has an unresolved hyperfine structure) and by the experimental results in molecular iodine vapor (angular momenta of the active levels are known, but  $J \gg 1$ ) [15]. Since it is difficult to record a weak echo signal against the background of wings of much more intensive excitation pulse signals, only the PE polarization components polarized orthogonally to the excitation pulses were studied in both abovementioned papers.

The angular PE technique used in the studies of the magnetic field effect on the SPE polarization [13–16] allowed the PE radiation beam to be separated from the excitation radiation pulses and thus it was possible to investigate both PE polarization components and to use them for restoration of the PE polarization vector behavior in gas at the  $J = 1 \leftrightarrow J = 0$  transition in the longitudinal magnetic field. The experimental results [16] showed considerable deviation from the simplified theoretical analysis that assumed shortness of the excitation pulses ( $T_i \ll \tau$ ). Therefore, later [13] more rigorous analysis was developed using numerical calculations (described herein) to consider the finite width of excitation pulses. This theoretical analysis provided acceptable semi-quantitative agreement with experimental data.

## 2.2. Theoretical analysis of PE in gas at the $0 \leftrightarrow 1$ transition in the presence of the longitudinal magnetic field

Degenerate resonance atomic energy levels  $E_b$  and  $E_a$  ( $\omega_0 = \frac{E_b - E_a}{\hbar}$ ) in a static magnetic field are split into magnetic sublevels:

$$E_{bm} = E_b + m\epsilon_b, \quad E_{a\mu} = E_a + \mu\epsilon_a, \quad (5)$$

where  $m$  and  $\mu$  are the projections of total angular momenta of levels  $J_b$  and  $J_a$  on the  $Z$  quantization axis taken in the excitation pulse propagation direction,

$$\epsilon_b = \frac{g_b \mu_B \mathcal{B}}{\hbar}, \quad \epsilon_a = \frac{g_a \mu_B \mathcal{B}}{\hbar}, \quad (6)$$

$g_b$  and  $g_a$  are  $g$ -factors of the levels,  $\mu_B$  is the Bohr magneton,  $\mathcal{B}$  is the magnetic field strength.

Interaction between the gas medium and excitation laser radiation pulses with electric field strengths

$$\mathbf{E}_n = \mathbf{e}_n \exp\{-i(\omega t - kz)\} + \text{c.c.}, \quad n = 1, 2, \quad (7)$$

where  $\mathbf{e}_n$  is the slowly varying amplitude represented by the following equation

$$\left(\frac{\partial}{\partial t} + \mathbf{v}\nabla\right) \hat{\sigma} = \frac{i}{\hbar} [\hat{\sigma}, \hat{H}_0 - \hat{\mathbf{d}}\mathbf{E}_n] \quad (8)$$

for the atom (molecule) density matrix  $\hat{\sigma}$ , where  $\mathbf{v}$  is the atom (molecule) velocity,  $\hat{H}_0$  is the free atom Hamiltonian,  $\hat{\mathbf{d}}$  is the electric dipole moment operator.

In the rotating wave approximation, we obtain the following equation:

$$\dot{\hat{\rho}} = i[\hat{\rho}, \hat{V}] \quad (9)$$

for a slowly rotating matrix  $\hat{\rho}$  components of which are defined by

$$\sigma_{mm'}^{bb} = \rho_{mm'}^{bb}, \quad \sigma_{\mu\mu'}^{aa} = \rho_{\mu\mu'}^{aa}, \quad \sigma_{\mu m}^{ab} = \rho_{\mu m}^{ab} \exp\{-i(\omega t - kz)\}, \quad (10)$$

and  $\hat{V}$  — square matrix  $2(J_b + J_a + 1) \times 2(J_b + J_a + 1)$  with components

$$(V_n)_{mm'}^{bb} = \delta_{mm'} \left(m\epsilon_b + \frac{\delta}{2}\right), \quad (V_n)_{\mu\mu'}^{aa} = \delta_{\mu\mu'} \left(\mu\epsilon_a - \frac{\delta}{2}\right),$$

$$\delta = kv + \omega_0 - \omega,$$

$$(V_n)_{m\mu}^{ba} = ((V_n)_{\mu m}^{ab})^* = -\frac{1}{\hbar} (\mathbf{d}\mathbf{e}_n)_{m\mu}^{ba} = \frac{d e_n}{\hbar\sqrt{2}} (-1)^{J_b - m}$$

$$\times \sum_q \begin{pmatrix} J_b & 1 & J_a \\ -m & q & \mu \end{pmatrix} (\delta_{q,1} \exp(-i\psi_n) - \delta_{q,-1} \exp(i\psi_n)).$$

(11)

Here  $v$  is the projection of the atom velocity on the  $Oz$  axis,  $d$  is the reduced matrix element of the electric dipole moment operator of an atom for the  $J_b \rightarrow J_a$  transition,  $3j$ -symbols are defined in a conventional manner,  $\psi_n$  is the

angle between the polarization vector of the  $n$ -th excitation pulse and the  $Ox$  axis.

Linear polarization excitation pulses will be considered hereinafter with the constant amplitudes  $e_n$  and widths  $T_n$  ( $n=1,2$ ). In this case, the solution of equation (9) may be as follows:

$$\hat{\rho}_n = \hat{S}_n \hat{\rho}_{n-1} \hat{S}_n^+, \quad (12)$$

where  $\hat{\rho}_{n-1}$  and  $\hat{\rho}_n$  are the atom density matrices before arrival and after transmission of the  $n$ -th excitation radiation pulse, and the evolution matrix is written as

$$\hat{S}_n = \exp(-iT_n \hat{V}_n). \quad (13)$$

The initial atom density matrix  $\hat{\rho}_0$  at a point of time before the first excitation pulse falls on the medium is written as

$$\hat{\rho}_0 = n_0 f(v) |J_a, \mu\rangle \langle J_a, \mu|, \quad (14)$$

where  $n_0$  is the resonant atom concentration,

$$f(v) = \frac{1}{\sqrt{\pi}u} \exp\left(-\frac{v^2}{u^2}\right) \quad (15)$$

is the Maxwell function of atom distribution by velocities,  $u$  is the average atomic thermal velocity.

The strength of the PE electric field

$$\mathbf{E}^e(t') = \mathbf{e}^e(t') \exp\{-i(\omega t' - kz)\} + \text{c.c.},$$

$$t' = t - z/c - T_1 - T_2 - 2\tau, \quad (16)$$

generated by the excitation pulses separated by the delay time  $\tau$  may be obtained from the Maxwell equation:

$$\left(\Delta - \frac{1}{c^2} \frac{\partial^2}{\partial t'^2}\right) \mathbf{E}^e = \frac{4\pi}{c^2} \frac{\partial^2}{\partial t'^2} Sp(\hat{\sigma}, \hat{\mathbf{d}}). \quad (17)$$

Projection of the slowly varying amplitude of the PE electric field  $\mathbf{e}^e(t')$  on the polarizer axis

$$\mathbf{l} = \mathbf{l}_x \cos \phi + \mathbf{l}_y \sin \phi, \quad (18)$$

forming the angle  $\phi$  with the  $Ox$  axis is equal to:

$$e^e(t') = (\mathbf{e}^e, \mathbf{l}) = i \frac{e_0}{\sqrt{\pi}} \int_{-\infty}^{\infty} \exp(-x^2 - ikut'x) F(x) dx,$$

$$e_0 = 2\pi\omega \frac{L}{c} n_0 |d| \exp(-2\gamma\tau), \quad (20)$$

$$F(x) = \sum_{m,\mu} G_{m\mu}(x) \exp\{-it'(m\epsilon_b - \mu\epsilon_a)\}, \quad (21)$$

$$G_{m\mu}(x) = \sum_{m',\mu',\mu''} \exp\{i\tau[\epsilon_b(m' - m) - \epsilon_a(\mu' - \mu)]\}$$

$$\times (\mathbf{g}, \mathbf{l})_{\mu m}^{ab} (\hat{S}_2)_{m\mu'}^{ba} (\hat{S}_2^+)_{m',\mu}^{ba} (\hat{S}_1)_{\mu',\mu''}^{aa} (\hat{S}_1^+)_{\mu'',m'}^{ab}. \quad (22)$$

Here  $L$  is the gas medium length,  $1/\gamma$  is the irreversible relaxation time that is assumed much higher than the

excitation pulse and echo pulse widths,  $\hat{\mathbf{g}} = \hat{\mathbf{d}}/|d|$ , and the matrices  $\hat{S}_n$  are determined by equation (13).

The experiments record a full echo pulse intensity transmitted through the polarizer that (in arbitrary units) is written as

$$\begin{aligned} I^e &= \frac{ku}{2e_0^2} \int_{-\infty}^{\infty} |e^e(t')|^2 dt' \\ &= \sum_{m,\mu,m_1,\mu_1} \int_{-\infty}^{\infty} dx \exp\{-x^2 - (x - \xi_{m\mu m_1 \mu_1})^2\} \\ &\times G_{m\mu}(x) G_{m_1 \mu_1}^*(x - \xi_{m\mu m_1 \mu_1}), \end{aligned} \quad (23)$$

where

$$\xi_{m\mu m_1 \mu_1} = \frac{1}{ku} \{\epsilon_b(m - m_1) - \epsilon_a(\mu - \mu_1)\}. \quad (24)$$

Matrix elements of  $\hat{S}_n$  in equation (22) may be calculated in the diagonal representation of  $\hat{W}_n = T_n \hat{V}_n$ . Mark the vectors  $|J_b, m\rangle$  and  $|J_a, \mu\rangle$  of the initial basis with index  $\nu$  generally taking  $2(J_b + J_a + 1)$  values so that  $|\nu = 0\rangle = |J_b, m = J_b\rangle, \dots, |\nu = 2J_b\rangle = |J_b, m = -J_b\rangle, |\nu = 2J_b + 1\rangle = |J_a, \mu = J_a\rangle, \dots, |\nu = 2J_b + 2J_a + 1\rangle = |J_a, \mu = -J_a\rangle$ .

Then

$$\langle \nu | \hat{S}_n | \nu' \rangle = \sum_j c_{j\nu}^{(n)} \left( c_{j\nu'}^{(n)} \right)^* \exp(-i\lambda_j^{(n)}), \quad (25)$$

where  $\lambda_j^{(n)}$  are the eigenvalues of  $\hat{W}_n$  and

$$c_{j\nu}^{(n)} = \langle \nu | u_j^{(n)} \rangle, \quad (26)$$

where  $|u_j^{(n)}\rangle$  are the corresponding eigen vectors.

In case of a weak magnetic field ( $|\epsilon_b - \epsilon_a| \ll ku$ )

$$I^e = \int_{-\infty}^{\infty} dx \exp(-2x^2) \left| \sum_{m,\mu} G_{m\mu}(x) \right|^2, \quad (27)$$

and in case of a strong magnetic field ( $\epsilon_b, \epsilon_a \gg ku$ )

$$I^e = \int_{-\infty}^{\infty} dx \exp(-2x^2) \sum_{m,\mu} |G_{m\mu}(x)|^2. \quad (28)$$

If PE is formed on a narrow spectral line, i.e.  $kuT_n \ll 1$ , then  $G_{m\mu}(x) = G_{m\mu}(0) = G_{m\mu}$  and

$$I^e = \sqrt{\frac{\pi}{2}} \sum_{m,\mu,m_1,\mu_1} G_{m\mu} G_{m_1 \mu_1}^* \exp\left(-\frac{1}{2} \xi_{m\mu m_1 \mu_1}^2\right), \quad (29)$$

where  $\xi_{m\mu m_1 \mu_1}$  is determined by equation (24).

Numerical calculations of the full PE intensity  $I^e$  were conducted in the precise resonance approximation for a transition with angular momenta  $J_a = 1 \leftrightarrow J_b = 0$ , for a wide

spectral line case ( $ku = 3.1 \cdot 10^9 \text{ s}^{-1}$ , which corresponds to the Yb vapor temperature of 800 K), for rectangular excitation pulses with the same widths  $T_1 = T_2 = 5.3 \text{ ns}$  and optimum areas  $\theta_1 = \pi/2$ ,  $\theta_2 = \pi$ , ( $\theta_n = \frac{2|d|e_n T_n}{\hbar\sqrt{3}}$ ) separated by the time interval  $\tau = 36 \text{ ns}$ . Numerical calculations using equation (22) and integration using equation (23) have been conducted in MathCad 8.01. The relations obtained numerically are shown dashed in the figures with the experimental data. Corresponding normalization of the experimental data has been performed for more convenient comparison of the numerical data with the experimental data. All main experimental behavior features of the PE polarization components in a magnetic field, including within a strong field, are reproduced by numerical calculations at a qualitative level.

### 2.3. Experiment technique for PE in a magnetic field

The first experimental setup used to study the non-Faraday polarization rotation of PE generated in gas at the  $0 \leftrightarrow 1$  optical transition in a longitudinal magnetic field is described in detail in [13].

The experimental setup is shown in Figure 3. A dye laser with optical pumping from an XeCl excimer laser with a radiation wavelength of 308 nm, radiation pulse width of 5–6 ns and average pulse energy of 20 mJ was used as a source of radiation generating PE in ytterbium vapor. To reduce the effect of fluctuations of the excimer laser power and spatial distribution inhomogeneity on the experimental data, measures were taken, including a special design of the dye laser and external optical setup, investigation of the output dye laser radiation and a special data acquisition method.

The dye laser design included a master oscillator with a resonator length of 10 cm and two serial amplification stages. Alcohol solution of Rhodamine 110 dye was slowly circulated in all cells. The resonator of the dye laser master oscillator was formed by a 1800 grooves/mm diffraction grating operating in the autocollimation mode with second-order diffraction, and by an output dielectric mirror. The diffraction grating placed in a vacuum chamber with controlled gaseous nitrogen pressure provided gradual radiation frequency tuning. An additional 1200 grooves/mm diffraction grating placed downstream of the master oscillator was used to cut off the spontaneous radiation of the dye cell.

Between the master oscillator and the first amplification stage and between the first and second amplification stages, spatial angular selectors were placed with each of them consisting of two positive lenses and a diaphragm between the lenses. Radiation from the beam center extracted by the diaphragm with a diameter of 1.5 mm and transmitted through the Kepler telescope (shown in Figure 3 downstream of the amplification stages) to expand the beam to a diameter of 10 mm was delivered to the external optical setup. The spatial angular selectors and

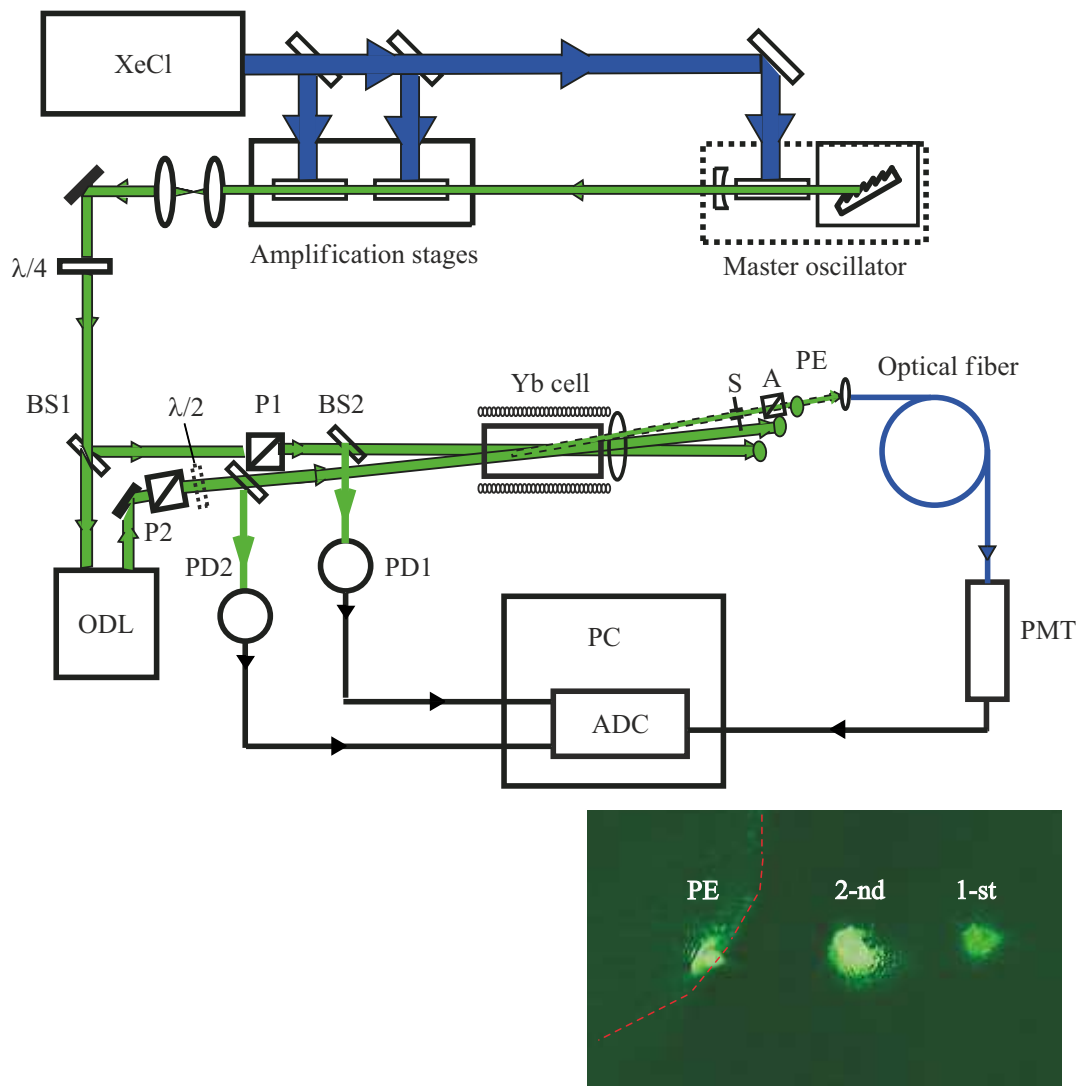


**Figure 3.** Experimental setup for investigation of a photon echo generated in ytterbium vapor at the  $0 \leftrightarrow 1$  transition in a longitudinal magnetic field. At the bottom — image of excitation beams weakened by a filter and of a PE signal.

telescopic beam expansion used in such manner made it possible to considerably decrease the background radiation associated with dye superfluorescence and to achieve quite homogeneous transverse beam distribution and divergence close to the diffraction limit.

The external setup included quarter-wave plate  $\lambda/4$ , plane-parallel plates BS1 and BS2 for beam splitting, optical delay line ODL to create a pair of coherent excitation radiation pulses separated by the delay time  $\tau$ , and two Glan–Taylor prisms P1 and P2 allowing the desired linear polarization to be chosen for each of the excitation radiation beams. Polarization of the second excitation radiation pulse may be rotated, if required, at  $90^\circ$  using half-wave plate  $\lambda/2$ . Film polarizer A placed downstream of the active cell made it possible to analyze the polarization of PE recorded by the quick-acting high-sensitivity PMT after transmission through the lens and optical fiber. Excitation radiation pulse powers

were controlled by photodiodes PD1 and PD2; signal from the first excitation pulse recorded by PD1 served also for actuation of the amplitude-to-digital converter (ADC) of the photon echo signal.

Yb vapor cell was placed inside the solenoid and could be used in a wide temperature range; metallic ytterbium with purity 0.999 and natural isotope content was used. The measurement data were obtained at 800 K.

This study used an angular echo setup known since the first experimental study of PE [5]. Relative location of the excitation radiation beams can be seen on the image of Creative WebCam 3 placed in the focal plane of lens L. This picture is shown in the insertion in right bottom corner of Figure 3. The excitation radiation beams are weakened by the light filter, filter boundaries can be seen; PE signal distribution is uneven due to partial overlapping by the light filter. When measuring, the PE beam passed

through slit S to ensure additional protection of PMT from the excitation pulse wings. An angle between the excitation pulse wave vectors was equal to  $1.8 \cdot 10^{-3}$  rad; this appeared to be sufficient for spatial extraction of the PE beam. At the same time, this angle was sufficiently small to avoid too high attenuation of the PE signal due to decrease of excitation radiation beam overlapping within the cell. The effect of the angle between the beams on the PE signal was assessed in [16] using the results of [17] and these assessments serve as the basis for the above statement.

The excitation radiation pulse powers had considerable fluctuations, therefore, PE instances formed by the excitation pulses with fluctuations higher than 10% of the average value were rejected by the software during data acquisition through ADC. For excitation pulse power fluctuations lower than 10%, the PE signals were normalized for the powers measured in this instance. Empirical dependences of the PE signals on the power of each of the excitation pulses appeared to be gradually increasing whereof it was suggested that the excitation pulse areas did not exceeded  $\pi/2$  for the first pulse and  $\pi$  for second pulse.

The experimental data given below were obtained by averaging over 30–40 successful (not rejected as mentioned above) PE pulses.

The dye laser radiation spectrum was studied using a 10 mm Fabry-Perot tunable interferometer; spectrum width averaged over 40 laser pulses appeared to be 3–4 GHz. This is a sufficiently low value for excitation of only even ytterbium isotopes with zero nuclear spin, i.e. without hyperfine active level structure. The interferogram of a single laser pulse transmitted through the interferometer showed a multimode structure containing one to four modes with an intermode distance of 1.5 GHz (longitudinal modes of the master oscillator); spectral width of each mode was assessed by the pulse width  $1/(2\pi T_i) \approx 30$  MHz.

It should be emphasized that the delay time  $\tau = 36$  ns is comparable with the excitation pulse width  $T_i = 5$  ns, therefore the approximation  $T_i \ll \tau$  is not applicable in our case, and the analytical theory results shall be provided with numerical count.

#### 2.4. PE polarization rotation in a „weak“ magnetic field

Polarization of PE generated at the  $(6s6p)^3P_1 \rightarrow (6s^2)^1S_0$  transition of  $^{174}\text{Yb}$  atoms in Yb vapor by two resonance radiation pulses with the same linear polarization in the presence of a weak longitudinal magnetic field  $\mathcal{B} \leq 5$  G was investigated at the first step. According to [11] (and references herein), PE shall retain the linear polarization and the echo polarization vector shall rotate clockwise around the magnetic field vector. When looking toward the  $-Oz$  direction, as in our experiment, the polarization plane shall rotate counterclockwise at an angle defined by the magnetic field strength, delay

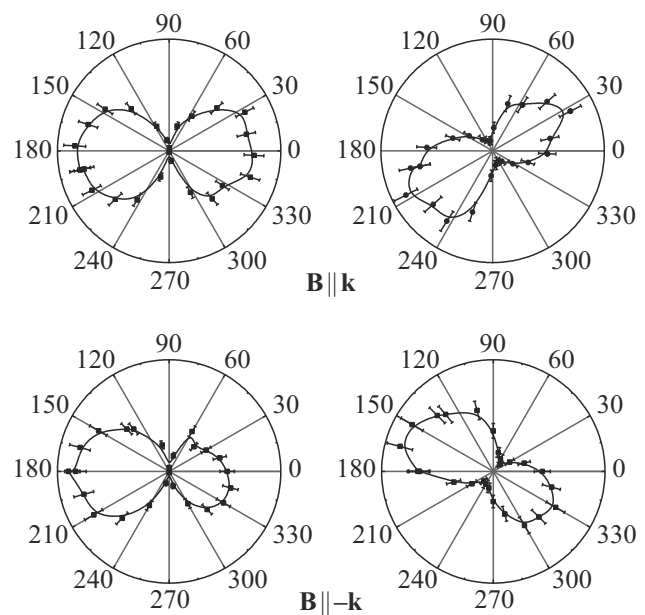


**Figure 4.** Polar plots of the second excitation pulse power and photon echo power in the 1.8 G magnetic field. The top right plot demonstrates the PE polarization plane rotation at  $30^\circ$  counterclockwise when looking toward the radiation propagation direction (in this case  $\mathbf{B} \parallel \mathbf{k}$ ). Sign reversal of the magnetic field ( $\mathbf{B} \parallel -\mathbf{k}$ ) results in rotation at  $30^\circ$  clockwise (right bottom plot).

time between the excitation pulses and optical transition properties.

To investigate the polarization of PE generated by the resonance radiation pulses with the same linear polarization at the  $(6s6p)^3P_1 \rightarrow (6s^2)^1S_0$  transition of  $^{174}\text{Yb}$  atoms in a 1.8 G weak magnetic field, power of the PE signal transmitted through the analyzer (placed upstream of the radiation recording PMT) were measured depending on the analyzer rotation angle. Similar measurements of the second excitation pulse power were conducted for comparison. The results are shown in Figure 4 as polar plots where the power of the measured light signal is plotted along the radius and the azimuthal angle corresponds to the analyzer rotation angle. Zero angle of the analyzer corresponded to the maximum signal of the linear polarization excitation pulses transmitted through an empty cell.

Experimental points in Figure 4 are connected by curves representing spline approximation. Note that the polar plots of the excitation pulses did not find any distinctive magnetic rotation, which is the evidence that there is no Faraday rotation of light pulses in Yb vapor. Asymmetry of the polar plot lobes of the second excitation pulse and PE power (lower row in Figure 4) is explained by slow decrease of the dye laser power due to the degradation of the excimer laser mixture used for dye laser pumping.

Polar plots of the photon echo power are shown in the right column in Figure 4. The top plot corresponds to the magnetic field that coincides with the excitation pulse wave vectors in direction. The axis of symmetry of this plot

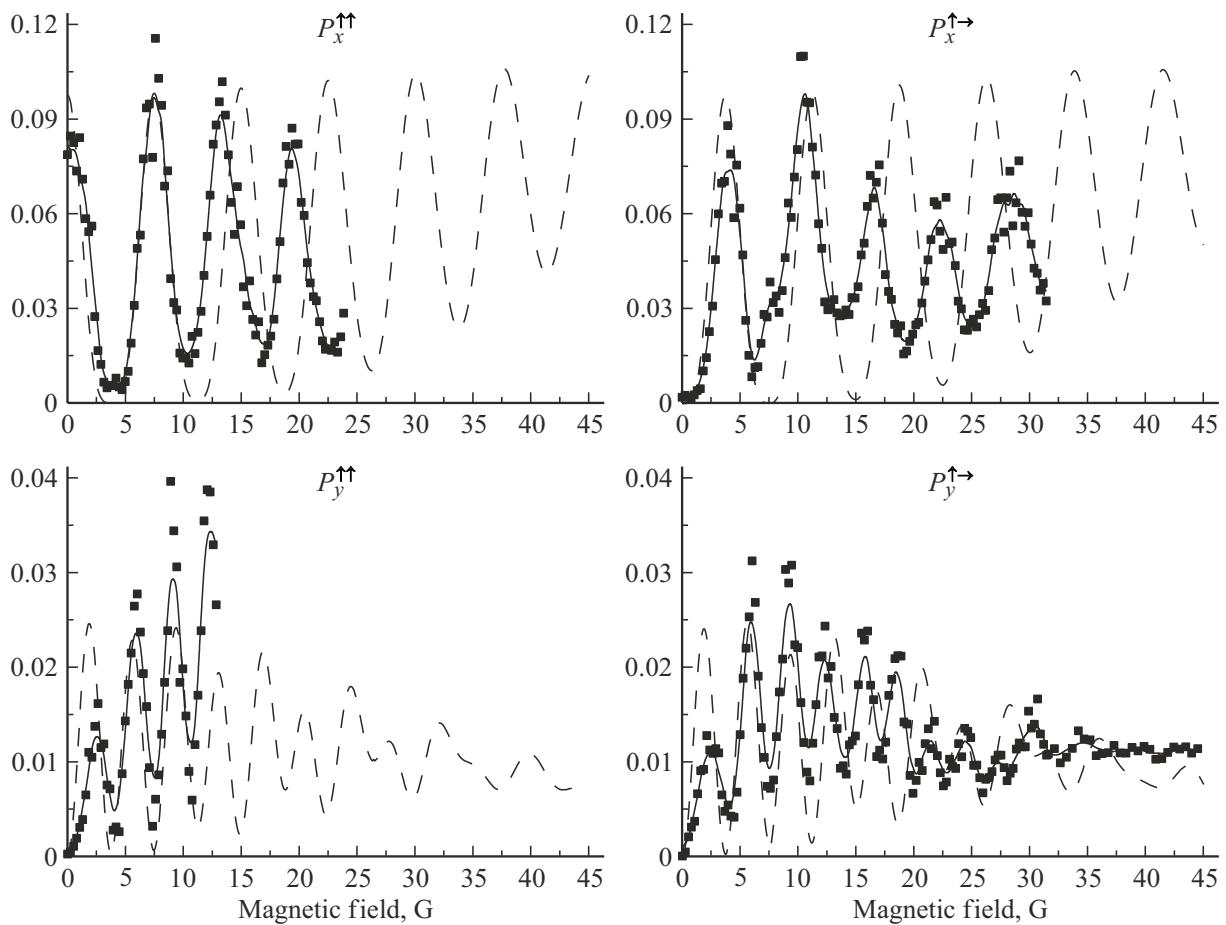


**Figure 5.** Oscillations of PE power generated in Yb vapor at the  $0 \leftrightarrow 1$  transition by a pair of excitation pulses with the same linear polarization (left) and cross polarization (right). Top — power of the PE component corresponding to the  $x$ -polarization, bottom — power of the PE component corresponding to the  $y$ -polarization. PE power oscillations for the  $y$ -polarization occur on a twice as higher frequency, minimum signal values grow in stronger magnetic fields and oscillations decrease at the limit. Numerical count results are shown dashed.

is rotated at  $30^\circ$  about the excitation pulse polarization direction. Reversal of the magnetic field direction to a direction antiparallel to the excitation pulse wave vectors (by reversal of the current flow in the solenoid coil) results in reversal of the photon echo polarization, which can be seen on the bottom right plot in Figure 4. The magnetic field strength is equal to 1.8 G in both cases. Both PE plots have narrow waists; this means that the photon echo polarization in a weak magnetic field is close to linear polarization.

### 2.5. Investigation in a wider magnetic field variation range

Then, behavior of the powers of  $x$ - and  $y$ -components of the PE polarization with magnetic field growth was investigated. Measurements were conducted for two cases: for PE generated by the excitation pulses with the same linear polarization (marked with  $\uparrow\uparrow$ ) and for the excitation pulses with mutual orthogonal linear polarizations (marked with  $\uparrow\rightarrow$ ).

Figure 5 on the left shows the results for the first case corresponding to the PE excitation by similarly polarized pulses (of  $\uparrow\uparrow$  type), and on the right — for the PE excitation by the cross linear polarizations of the excitation pulses ( $\uparrow\rightarrow$ ). Power oscillations are clearly seen as the magnetic field strength  $\mathcal{B}$  grows both for the  $x$ -component and the  $y$ -component for both combinations of excitation pulse polarizations. Each point on the plot was obtained for a fixed field strength, for a certain rotation angle of analyzer A and represents the result of averaging over 40 successful instances (i.e. over 40 laser pulses with allowable power deviation of each of the pulses). Smooth lines are given for better visualization and represent fitting of the experimental data by 5 neighboring points on the curve; numerical count results are shown dashed. Power oscillation frequency of the  $P_y^{\uparrow\uparrow}$   $y$ -component of the PE polarization is twice as high as that of the  $P_x^{\uparrow\uparrow}$   $x$ -component of the polarization for PE generation by pulses with the same linear polarization; the same is also true for the power oscillation frequencies  $P_x^{\uparrow\rightarrow}$  and  $P_y^{\uparrow\rightarrow}$  for PE generation by the mutually orthogonal

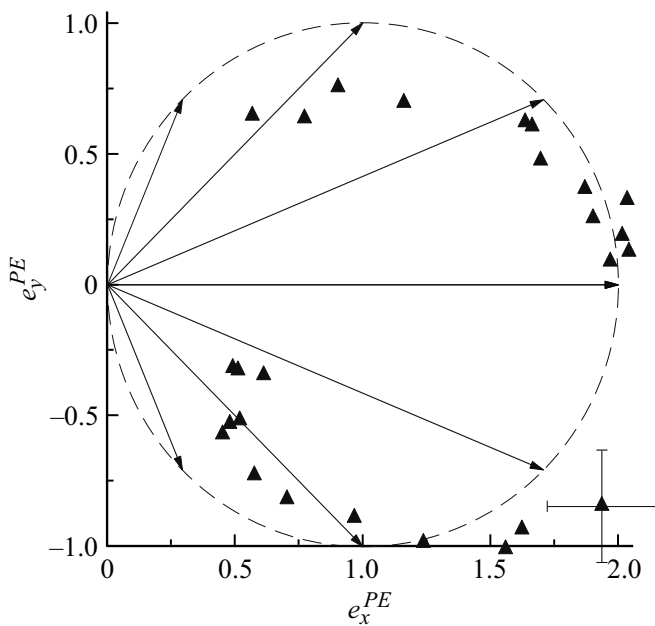


**Figure 6.** Evolution of the PE electric field amplitude in gas at the  $0 \leftrightarrow 1$  transition in a weak magnetic field; triangles show the data restored from the measurements; a dashed circle — is a simplified theory result (identical to Figure 2). When PE is excited by the resonance radiation pulses with the same linear polarization ( $\uparrow\uparrow$ ), the PE electric field vector in a zero magnetic field is horizontal and has a maximum length. As the magnetic field strength grows, the vector rotates and decreases to zero and then returns to the initial value circumscribing a circle by its end. The circle is shown dashed. When PE is excited by pulses with linear cross polarizations ( $\uparrow\rightarrow$ ), the PE electric field vector starts from zero, then its length gradually grows and decreases in such a way that the PE electric field vector end circumscribes the same circle.

linear polarizations of the excitation pulses. As the magnetic field strength grows, separation of the minimum signal values from zero and oscillation attenuation can be seen. Such behavior does not fit in a simplified theoretical analysis format (neglecting the excitation pulse width) and is in good qualitative agreement with the numerical calculations. Note that there are no PE signals in the zero magnetic field for PE generation by the cross polarization pulses  $\uparrow\rightarrow$  (this can be seen on the curves in the right column in Figure 5), which proves low contribution of depolarizing collisions, i.e. correct selection of gas pressure conditions for this series of experiments.

Key features of the PE signal behavior in a longitudinal magnetic field are generally well reproduced by calculations. Deviations in the amplitudes of measured and calculated signal values in Figure 5 are not a surprise bearing in mind the laser power instability of the excitation pulses and possible instability of the excitation laser radiation frequency (calculations were conducted for the precise resonance with the chosen optical transition), taking into account long recording time of each curve reflecting the

effect of magnetic field strength. Spatial inhomogeneity of the excitation radiation beams that is well seen in the detail in Figure 3 and magnetic field inhomogeneity also serve as the sources of deviations between the experimental data and calculations. Considering all these remarks, it is arguable that the calculation data is in satisfactory agreement on the qualitative level with the experimental data for the PE signal dependence on the longitudinal magnetic field strength.

Oscillation data of the polarization PE components in the weak magnetic field area ( $\mathcal{B} \leq 5$  G) was used to determine the  $g$ -factor of the upper active level  $g = (1.48 \pm 0.11)$ , which coincides with its theoretical value 1.5.

PE electric field amplitudes  $e_x^{PE}$  and  $e_y^{PE}$  were restored from the first PE oscillation period; their relative values in accordance with equations (1) and (2) give an idea of the PE electric vector evolution during rotation in a weak magnetic field. The results are shown in Figure 6 in the form of experimental values (triangles); measurement error is shown for one experimental point in the right bottom part of the figure; a dashed curve shows the predicted simplified theoretical analysis.

When PE is excited by the resonance radiation pulses with the same linear polarization  $\uparrow\uparrow$ , the PE electric field vector in a zero magnetic field is horizontal in Figure 6 and has a maximum length. As the magnetic field strength grows, the vector rotates and decreases to zero and then returns to the initial value circumscribing a circle by its end. The circle is shown dashed.

When PE is excited by the pulses with linear cross polarizations  $\uparrow\rightarrow$ , the PE electric vector starts from zero, then its length gradually grows with its end passing along the same circle. Thus, taking into account the measurement accuracy, the experimental data obtained for PE in gas at the  $0 \leftrightarrow 1$  transition within the weak longitudinal magnetic field are in satisfactory agreement with the simplified theoretical analysis data.

## 2.6. „Non-polarized“ PE in a „strong“ magnetic field

In a „strong“ magnetic field area, about 40 G in our conditions, the PE signal has a perceptible power, however, oscillations of the photon echo polarization component power are almost not visible; this is well shown on the curve at the bottom of Figure 5. We investigated the polarization of PE generated in conditions of the cross linear polarizations of the excitation pulses in a  $\mathcal{B} \approx 40$  G longitudinal magnetic field. Measurements of PE signal power depending on the analyzer angle placed upstream of the radiation detector are shown in Figure 7 in the form of a polar plot where the echo signal power is plotted on the radius and the azimuthal angle corresponds to the analyzer angle.

Figure 7 shows the experimental points as black boxes, signal amplitude measurement error is shown as straight line segments oriented along the radius, analyzer angle error is

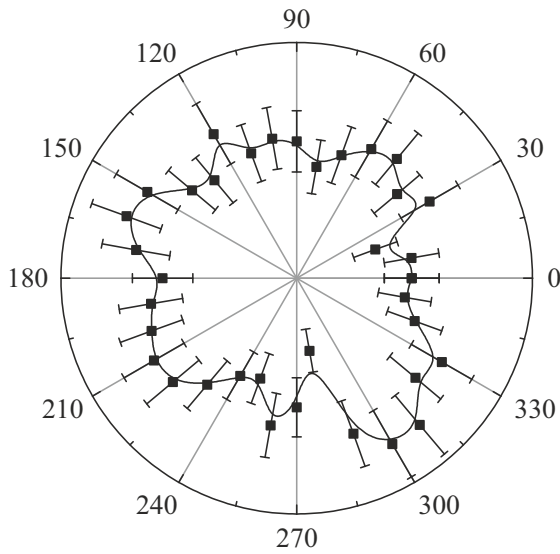


**Figure 7.** Polar plot of PE power (the PE power transmitted through the analyzer is plotted on the radius, the azimuthal angle is the analyzer angle) generated by the resonance radiation pulses with linear cross polarizations in the  $\mathcal{B} \approx 40$  G magnetic field. The photon echo does not disappear, but has no preferential polarization orientation.

low on a scale of the experimental points; a thin smooth line passing through the experimental points is shown for visualization and is a B-spline approximation. Thus, the PE polar plot in Figure 7 considering the measurement accuracy has no preferential direction.

**2.7. Findings of the PE study in gas at the  $0 \leftrightarrow 1$  transition in a magnetic field**

Summarizing the findings of the study of the non-Faraday PE polarization rotation at the  $0 \leftrightarrow 1$  transition in Yb vapor, two ranges of the longitudinal magnetic field strengths, where this phenomenon appears to be different, may be distinguished.

In case when PE is generated by the resonance radiation pulses with the same linear polarizations ( $\uparrow\uparrow$ ) within a weak magnetic field, the  $x$ -component of polarization is maximum and the  $y$ -components is equal to zero in a zero magnetic field. As the magnetic field strength grows, the PE polarization remains linear and the PE polarization vector rotates around the magnetic field vector  $\mathbf{B}$  at an angle proportional to  $\frac{\mu g \mathcal{B} \tau}{\hbar}$ . This results in the oscillations of the  $x$ -  $y$ -components of the PE polarization depending on the magnetic field strength. When PE is generated by the excitation pulses with cross linear polarizations ( $\uparrow\rightarrow$ ), there is no PE in a zero magnetic field, and this fact proves that contribution of the depolarizing collisions is low in the chosen experimental conditions. As the magnetic field strength grows, the PE polarization behavior is similar to the  $\uparrow\uparrow$  excitation case.

As follows from the simplified theoretical consideration (equation (1)–(4)), the delay time between the excitation pulses  $\tau$  and the magnetic field strength  $\mathcal{B}$  have the same influence on the rotation angle. It could be expected that the increased delay time and magnetic field strength growth shall affect the PE polarization rotation in the same manner as shown experimentally in [14]. However, this is true only within a weak magnetic field. Generally, the increase in  $\tau$  and  $\mathcal{B}$  is not equivalent. The growth of  $\tau$  may only improve the applicability conditions of the simplified theoretical analysis  $T_i \ll \tau$ , while the magnetic field strength  $\mathcal{B}$  is an essential variable of the problem because its growth may change the measurement in a qualitative manner — PE may acquire polarization ellipticity due to a possible excitation asymmetry of the Zeeman sublevels  $M = -1$  and  $M = +1$  of the upper active state. The abovementioned asymmetry may occur in our experiments due to unstable dye laser radiation frequency.

In a stronger magnetic field, oscillations of the  $x$ - and  $y$ -components of the PE polarization decrease by amplitude and disappear. This „strong“ magnetic field limit corresponds to  $\frac{\mu g \mathcal{B}}{\hbar} \gg \frac{1}{T_i}$ . On the one hand, this means that the spectral width of excitation pulses becomes low compared with the Zeeman splitting. On the other hand, this corresponds to the case when the echo response duration is long compared with the echo polarization plane rotation period in a magnetic field. In case when there is a considerable offset of the excitation radiation frequency from the transition center, a situation is possible when only one of the upper level Zeeman sublevels ( $M = 1$  or  $M = -1$ ) is excited and a circular PE polarization occurs; this shall result in a perceptible drop of the PE power, which was not observed in our experiments. Weak offset of the excitation radiation frequency from the transition center should result in an elliptical PE polarization with the major axis of ellipse rotating around the magnetic field vector, whereas the rotation frequency would be quite high for several turns during the echo pulse time. Fluctuations of the excitation radiation frequency offset in our experiments prevented from observing this transition from the linear PE polarization to the elliptical echo polarization. However, even for more stable radiation, the precise resonance case should result in generation of linearly polarized PE in a strong magnetic field with rotation of the polarization plane around the magnetic field vector at a sufficiently high speed to perform several complete turnovers during the echo pulse time. In view of these considerations, it is arguable that PE recorded experimentally within the strong longitudinal magnetic field [13] is actually non-polarized.

### 3. Stimulated photon echo generated in gas at the $0 \leftrightarrow 1$ transition in a longitudinal magnetic field

#### 3.1. SPE polarization calculations in a weak magnetic field

Calculation [12] of the strength  $\mathbf{E}^{SPE}$  of a SPE electric field formed at the  $0 \leftrightarrow 1$  transition by three resonance radiation pulses that propagate in the  $Oz$  direction and whose width  $T$  is small compared with the delay times  $\tau_{12}$  and  $\tau_{23}$ , and polarizations are linear and oriented along the  $Ox$  axis predicts periodic oscillations of the  $E_x^{SPE}$  and  $E_y^{SPE}$  components in a weak longitudinal magnetic field according to the following law:

$$E_x^{SPE} \propto \frac{2}{9} [\cos^2(\varepsilon_a \tau_{12}) + \cos^2(\varepsilon_a (\tau_{12} + \tau_{23}))], \quad (30)$$

$$E_y^{SPE} \propto \frac{1}{9} [\sin(2\varepsilon_a \tau_{12}) + \sin(2\varepsilon_a (\tau_{12} + \tau_{23}))]. \quad (31)$$

In equations (30) and (31), as before,  $\varepsilon_a = \mu g_a B / \hbar$  characterizes the Zeeman splitting by the magnetic field  $B$  of the upper active level with the  $g$ -factor  $g_a$ . It follows from expressions (30) and (31) that the  $y$ -component of SPE can occasionally vanish showing biharmonic oscillations as the magnetic field grows: at the same time, the  $x$ -component and the SPE electric field can generally  $E_{SPE} = \sqrt{(E_x^{SPE})^2 + (E_y^{SPE})^2}$  vanish only in case of particular ratios between  $\tau_{12}$  and  $\tau_{23}$ . Similar to PE at the  $0 \leftrightarrow 1$  transition, we construct picture of possible SPE electric field vectors in the presence of a longitudinal magnetic field.

Each point on the diagram, Figure 8, represents the end of the SPE electric vector  $\mathbf{E}_{SPE}$ , whose origin is in the origin of coordinates. Note that all rational ratios between  $\tau_{12}$  and  $\tau_{23}$  provide closed vector end paths when the magnetic field varies as a parameter. The delay ratio is equal to 1:2 on the top diagram, Figure 8, and to — 1:4 on the middle diagram. In case when SPE is generated by three light pulses polarized along the  $Ox$  axis, evolution of the SPE electric field vector starts in point corresponding to the maximum value of  $E_x$  and zero value of  $E_y$  (in the rightmost point on the diagram). As the magnetic field grows, the non-Faraday rotation of the SPE electric field vector occurs. In contrast to PE, the SPE electric field vector moves along a more complex looplike path as the magnetic field grows. On the top diagram in Figure 8, SPE vanishes after one looplike path, on the middle diagram in Figure 8 SPE becomes zero after two looplike movements of the vector. When  $\tau_{12} : \tau_{23}$  is higher, the number of loops on the path of the SPE electric field vector towards the first zero value may be even higher, but it is always possible to find a value of  $\tau_{23}$  and a set of magnetic field strengths  $B$  for the given value of  $\tau_{12}$ , for which vanishing of SPE is possible.

When  $\tau_{12}$  and  $\tau_{23}$  are not the best possible in term of SPE vanishing, behavior of the SPE vector is different. For example, when  $\tau_{12} : \tau_{23} = 1:1$ , the SPE signal does not

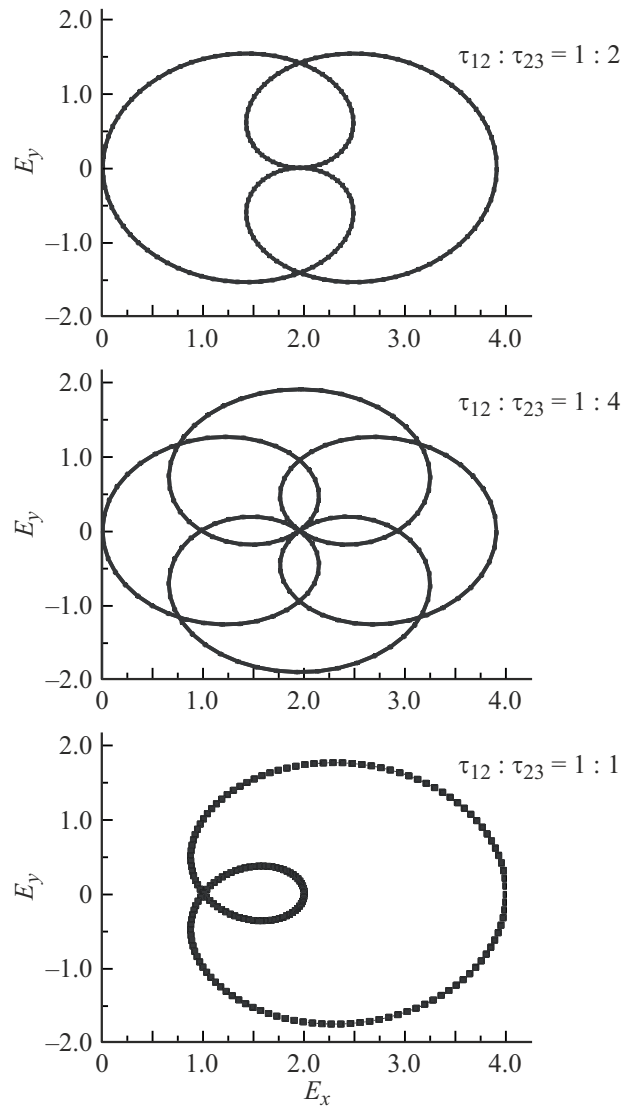


**Figure 8.** Diagrams of possible SPE electric field vectors (origin of the vector coincides with the origin of coordinates, the end is in the point on the diagram defined by the magnetic field strength and the delay times) at the  $0 \leftrightarrow 1$  transition in a longitudinal magnetic field for various delay time ratios between the excitation pulses; top —  $\tau_{12} : \tau_{23} = 1 : 2$ , middle —  $\tau_{12} : \tau_{23} = 1 : 4$ , bottom —  $\tau_{12} : \tau_{23} = 1 : 1$ .

vanish at any magnetic field strengths. This SPE diagram is shown at the bottom of Figure 8. When  $\tau_{12} > \tau_{23}$ , the SPE diagrams in the magnetic field may be more intricate. However, the first two excitation pulses in SPE-based data processing systems are usually close in time and form a signal code, while the reading process is put off in time, so  $\tau_{12} < \tau_{23}$  and even  $\tau_{12} \ll \tau_{23}$  are more typical.

#### 3.2. Experimental setup for study of SPE in ytterbium vapor

Our experiments used ytterbium with a natural isotopic composition, i.e. with prevailing concentration of stable

even isotopes (168, 170, 172, 174, 176) of about 69.5%. The dye laser radiation frequency was set to the center of the Doppler-broadened intercombination transition  $(6s6p)^3P_1 \rightarrow (6s^2)^1S_0$  of  $^{174}\text{Yb}$ . This isotope has the highest concentration in the natural ytterbium composition and the zero nuclear spin ensures that there is no hyperfine level structure. To obtain ytterbium vapors a tailor-made stainless steel cell was designed [13]. It was surrounded by a double-wound heater to avoid a spurious magnetic field from the heater inside the cell. A magnetic field was created in the cell by a solenoid whose length was greater than the cell length in order to minimize the spatial magnetic field inhomogeneity due to edge effects. The magnetic field amplitude was determined by the solenoid current. The design of the heated ytterbium vapor cell provided homogeneous density of vapor in the center. Temperature in the center of the cell was normalized to 830–840 K using a thermocouple and semistor current control of the heater.

Rhodamine 110 dye laser with a wavelength of  $\lambda = 555.6$  nm and optical pumping from XeCl laser (radiation wavelength 308 nm, pulse width 10 ns, pulse energy about 50 mJ) was used as a source of radiation. Its configuration is shown in detail in the section devoted to the study of PE in a longitudinal magnetic field. The spatial angular selectors and telescopic expander were used to reduce the background formed by the dye superradiance and to form a radiation beam with sufficiently homogeneous transverse distribution and divergence close to the diffraction one. The measurement using the FEK-22 quick-acting coaxial photocell have shown that the generation pulse width and shape do not sustain any perceptible fluctuations. The pulse has a smooth shape with a little steeper leading edge. However, the light pulse power sustains perceptible fluctuations.

The dye laser spectrum was occasionally controlled using a  $\lambda$ -meter with the laser set to the maximum ytterbium fluorescence signal at the  $(6s6p)^3P_1 \rightarrow (6s^2)^1S_0$  transition (corresponding to the center of the  $^{174}\text{Yb}$  line). The  $\lambda$ -meter is a set of Fabry-Perot interferometers with various gauge lengths (the largest one corresponds to a 12 mm quartz standard). The interference patterns of each of the interferometers are recorded using photodiode matrices whose signals arrive to a multichannel ADC and then to a computer for further processing. The computer makes graphical interference patterns and determines the center of spectral distribution for each individual laser generation pulse.

External experimental setup for the study of SPE polarization in ytterbium vapor at the  $(6s6p)^3P_1 \rightarrow (6s^2)^1S_0$  transition of  $^{174}\text{Yb}$  in a longitudinal magnetic field is described in detail in [18,19] and shown in Figure 9.

The excitation radiation pulses from Rhodamine 110 dye laser pumped by the XeCl excimer laser were formed by beam division into three parts using a dielectric beam splitting mirror system; then two beams were transmitted through independent spatial delay lines ODL2 and ODL3. All three beams were combined in the active cell at small

angles as mentioned above. Ratio of the serial excitation pulse powers was 1:1:1.8. With excitation radiation pulse widths  $T=10$  ns, delays between pulses were  $\tau_{12} = 23$  ns and  $\tau_{23} = 20$  ns, therefore the standard theoretical short pulse approximation was not satisfied. The same linear polarization of all three light pulses was provided using Glan prisms placed in each of the beams, and was controlled using the polarization plots at the active cell outlet. Similarly, the polarization plots were used to control the absence of pulse depolarization in the active ytterbium vapor cell windows and the absence of the trivial (Faraday) rotation of the radiation polarization when passing through the active ytterbium vapor cell.

Amplitude of each of the excitation pulses was measured by an avalanche photodiode and used for the primary data selection. Data collection was performed in real time with rejection of signals generated by the excitation pulses having an amplitude deviation more than by 10% with respect to some set values; SPE signals from 30–40 laser pulses corresponding to this rejection criterion were accumulated and averaged.

Polarization of SPE generated in Yb vapor at the  $0 \leftrightarrow 1$  transition by three laser pulses with the same linear polarization was studied experimentally in the angular echo setup with excitation pulse wave vectors oriented along triangular pyramid edges [19] as shown on top of Figure 10. The image recorded by a webcam placed in the focal plane of lens L shows cross-sections of the excitation pulse beams (1–3), angular PE generated by excitation pulses 1 and 3 (conventional two-pulse PE) and SPE signal. Small apex angle of the pyramid ensured spatial separation of SPE from the PE signals and from the excitation pulses, which is more important. The optical fiber end, that was used to deliver the light pulse to the PMT inlet, was insufficiently small in diameter for the spatial selection of the echo signal. Therefore a 0.2 mm diaphragm was additionally installed upstream of the optical fiber for selective SPE recording. SPE signal loss due to incomplete spatial overlapping of the excitation pulses was minimized when using small angles between the excitation pulses of  $\sim 1.8 \cdot 10^{-3}$  rad in this experiment.

### 3.3. SPE polarization in Yb vapor in a longitudinal magnetic field

The PE and SPE signals are known to be sensitive to the excitation radiation pulse areas proportional to the Rabi frequencies and pulse widths. SPE calculations conducted for the near-optimal ratio of three pulse areas  $\theta_1 : \theta_2 : \theta_3 = 3 : 3 : 4$  within  $\theta_1 = (0-16)\pi$  that was used for the experiment have shown that the dependence of SPE amplitude on  $\theta_1$  has a form of gradually increasing curve with superimposed oscillations. The calculations also assumed  $T_i = 10$  ns ( $i = 1, 2, 3$ ),  $\tau_{12} = 23$  ns,  $\tau_{23} = 20$  ns — in accordance with time-response characteristics of the excitation radiation used for the experiment. In accordance with the calculation, the SPE peaks shall be observed at

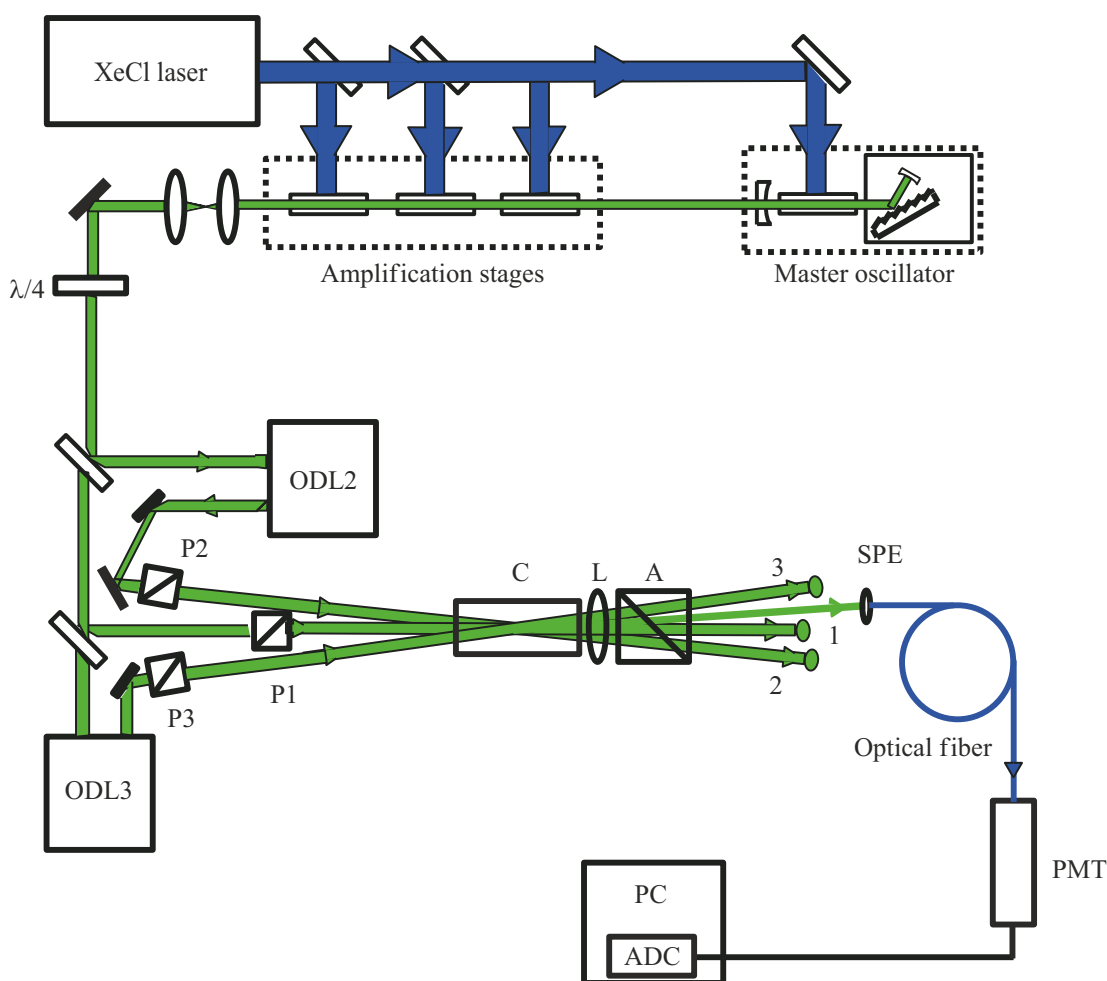


**Figure 9.** Experimental setup for the study of SPE polarization in a longitudinal magnetic field. The setup contains the pumping XeCl excimer laser, dye laser consisting of a master oscillator and three amplification stages; formation of the second and third excitation pulses using optical delay lines ODL2 and ODL3; polarizers P1-P3 providing the desired linear polarization of each of three pulses; ytterbium vapor cell C; lens L to focus the SPE radiation into the optical fiber, PMT for SPE recording; ADC for signal digitalization and PC.

the first pulse areas  $\theta_1 = (n + 1/2)\pi$  ( $n = 0, 1, \dots$ ). SPE achieves its highest values at  $\theta_1$  equal to  $8.5\pi$ ,  $11.5\pi$  and  $14.5\pi$ , whereas the echo amplitude is approximately thrice as high as the amplitude of the first peak observed at  $\theta_1 = 0.5\pi$ .

When studying the echo polarization properties, it is important to avoid the effect of depolarizing collisions. Therefore the experiment used as low ytterbium pressures as was allowed by the recording instruments. Reduction of the ytterbium pressure also reduces the risk of ytterbium sputtering on the active cell windows. Therefore, it was necessary to increase the laser radiation power for reliable SPE recording. The first excitation pulse area calculated by the measured light beam intensity and the ytterbium transition dipole moment known from the literature [20,21] was equal to  $11.5\pi$ .

To study SPE polarization, dependence of the SPE power on the angle of the analyzer located downstream of the active cell upstream of the radiation detector was recorded.

Such measurement results represented in polar coordinates are shown in Figure 11: in the zero magnetic field (a curve with the vertical axis of symmetry) and in the weak magnetic field  $B = 1.8$  G (axis of symmetry of this curve is rotated approx. at  $30^\circ$ ). The SPE polar plot in a zero magnetic field (experimental points in the form of black circles) has a narrow waist; this proves that SPE has a near-linear polarization in these experimental conditions. The SPE polar plot in the  $B = 1.8$  G magnetic field in Figure 11 (experimental points in the form of unshaded triangles) demonstrates the SPE polarization plane rotation around the magnetic field vector. The SPE polar plot waist in the magnetic field  $B = 1.8$  G is much larger than in the zero magnetic field. Note that the SPE signal depolarization appeared to be more distinctive than for the PE signal with the same magnetic field strength.

Behavior of the power of the  $x$ -component  $P_x^{SPE}$  and of the power of the  $y$ -component  $P_y^{SPE}$  of SPE with variation of the magnetic field is shown in Figure 12.

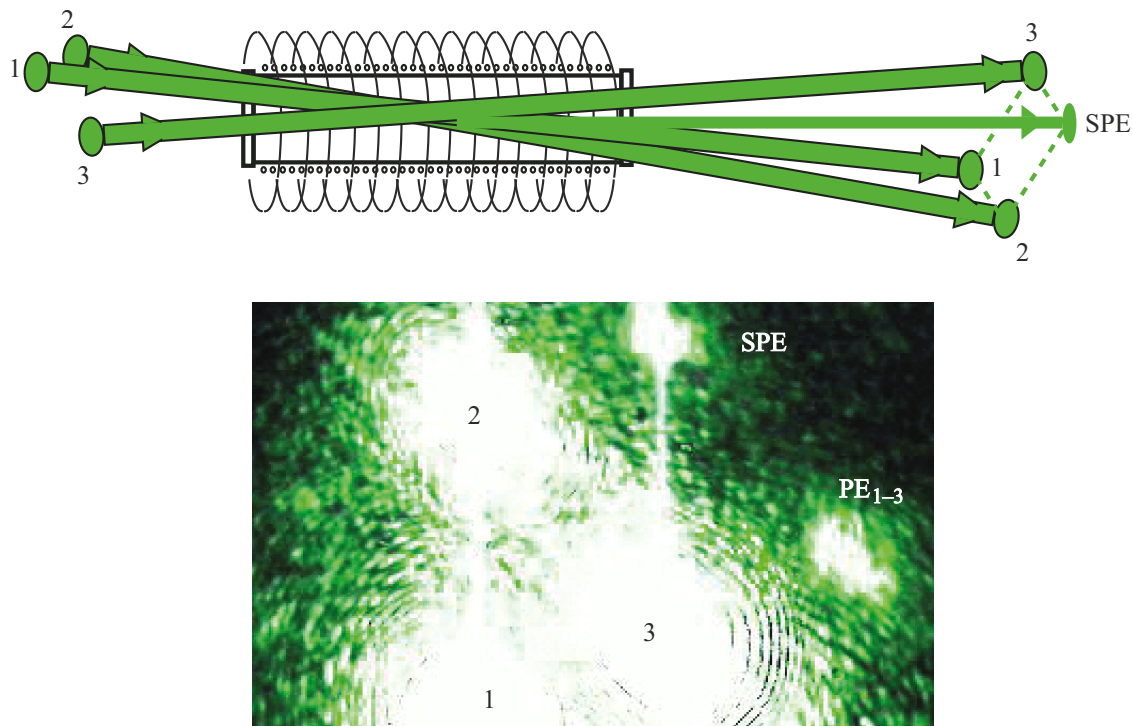


**Figure 10.** Angular SPE recording diagram. Top — arrangement of the resonance excitation radiation beams for angular SPE; bottom — picture of excitation beams (1, 2, 3) and SPE in a focal lens plane.

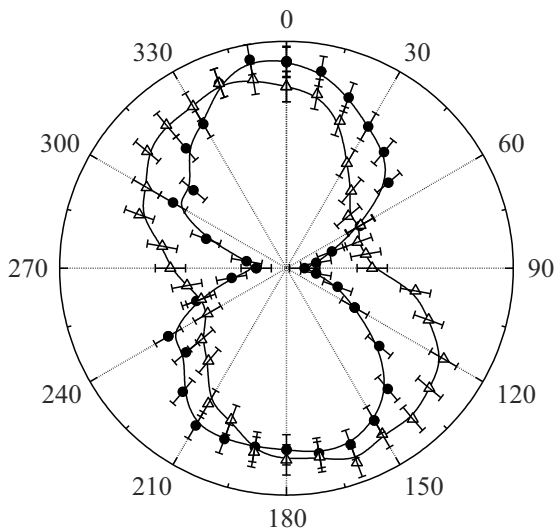


**Figure 11.** Non-Faraday SPE rotation in the magnetic field; black circles — SPE polar plot in the zero magnetic field, unshaded triangles — SPE polar plot in the magnetic field  $B = 1.8$  G.

Periodic biharmonic oscillations are only observed in small fields. As the field grows, the periodicity is deteriorated, SPE component oscillations become less distinctive and permanently disappear in a strong magnetic field. The dashed lines in Figure 12 correspond to the numerical calculations of the SPE polarization component power for

the excitation pulse area ratio 3:3:4 with the area of the first two pulses equal to  $11.5\pi$ .

Our experimental study of the SPE polarization in the longitudinal magnetic field did not pursue an objective to choose the best delay ratio that facilitated SPE vanishing. The experimental delay ratio was  $\tau_{12} : \tau_{23} = 23 : 20 \approx 1 : 1$ , so it should be expected that the SPE signals would not vanish with variation of the magnetic field.  $T \ll \tau_{12}$  and  $T \ll \tau_{23}$  were not satisfied either, thus equations (30) and (31) were strictly speaking not applicable, therefore numerical calculation was conducted taking into account the finite widths of the excitation pulses and the excitation radiation pulse areas that are close to the experimental values.

Similar to the PE case, the SPE polarization in the strong magnetic field does not show any preferential direction.

#### 4. Discussion

The previous overview [22] was mainly focused on the interconnection between depolarizing collisions and polarization properties of PE and SPE. Accordingly, applicability of the polarization echo spectroscopy methods for the study of depolarizing collisions was demonstrated. All experiments overviewed in [22] focused compensation of a laboratory magnetic field and Earth's field during measurements. For example, when investigating the signals of collision-induced SPE in the longitudinal magnetic field,

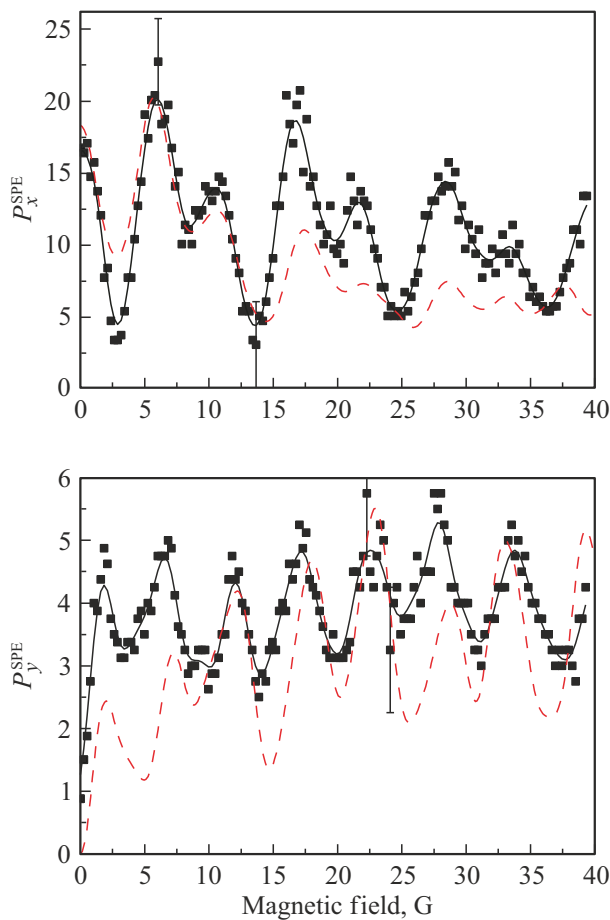


**Figure 12.** Dependence of the power of the SPE polarization components  $x$  (top) and  $y$  (bottom) on the magnetic field, biharmonic oscillations in the small field area and oscillation disappearance in the strong magnetic field can be seen.

field strength variation by 0.09 G resulted in a recorded variation of the echo response signal [23].

This overview shows the significant extent to which the magnetic field can influence the PE and SPE polarization; limiting cases of a „weak“ and „strong“ magnetic field are considered. For the experiments described herein, the magnetic field strength was varied within 0–45 G in 0.25 G steps, and the laboratory magnetic field with a strength of approx. 0.015 G was compensated.

As pointed out in subsections devoted to the experiment technique, it was necessary to consider the power and carrier frequency instability of the excitation laser pulses for data acquisition — for this data rejection was used. The model calculations did not consider the abovementioned frequency and amplitude instability of the excitation pulses. The theoretical analysis used the plane wave approximation, i.e. inhomogeneous transverse distribution of the excitation radiation intensities was neglected. Also, the spatial inhomogeneity of magnetic field was not considered, but the experiment included provisions to minimize the edge effects of the solenoid inducing the magnetic field in the ytterbium

vapor cell. This overview provides the calculation results considering the finite width of the rectangular resonance radiation excitation pulses; the experimentally recorded radiation pulses differ from the rectangular pulses. These circumstances may explain some discrepancy between the theoretical and experimental curves representing the dependence of the PE and SPE polarization component power on the magnetic field. However, the calculation curves generally reasonably reproduce the experimental data behavior with the growth of magnetic field.

## 5. Conclusion

The uniqueness of the  $0 \leftrightarrow 1$  transition is in that the non-Faraday rotation of the PE and SPE polarization plane in the weak magnetic field is followed by magnetic-field-periodic vanishing of the coherent response. For PE, this is observed the more distinctively the shorter excitation radiation pulses are compared with the delay time interval between them. In addition, it is necessary for SPE to choose correctly the ratio of  $\tau_{12}$  and  $\tau_{23}$ . Such vanishing of the coherent responses in the magnetic field makes it possible to control the data storage, recording and erasing processes. Within the weak longitudinal magnetic field, the polarization vectors of PE and SPE induced by the linear polarization radiation pulses may be rotated at the desired angle. Within the weak magnetic field, the coherent response polarization shall be still close to linear polarization.

The PE and SPE polarization state in the strong magnetic field is also of interest. The radiation detector response rate prevented recording of the internal polarization structure of PE and SPE. Since the non-Faraday polarization rotation process is reversible, it is suggested that the „nonpolarized echo“ phenomenon will be suitable for coding and recovery of data encrypted in the radiation polarization state.

## Conflict of interest

The authors declare that they have no conflict of interest.

## References

- [1] N.W. Carlson, L.J. Rothberg, A.G. Yodh, W.R. Babbitt, T.W. Mossberg. *Optics Letters*, **8** (9), 483 (1983).
- [2] I.V. Yevseyev, V.M. Yermachenko, V.V. Samartsev. *Depolarizing collisions in quantum electrodynamics* (CRC Press, Boca Raton, London, New York, Washington, 2004)
- [3] I.V. Evseev, N.N. Rubtsova, V.V. Samartsev. *Kogerentnye perekhodnye protsessy v optike* (Fizmatlit, Moskva, 2009).
- [4] T. Wang, C. Greiner, J.R. Bochinski, T.W. Mossberg. *Phys. Rev. A*, **60**, R757 (1999). DOI: 10.1103/PhysRevA.60.R757
- [5] N.A. Kurnit, I.D. Abella, S.R. Hartmann. *Phys. Rev. Lett.*, **13**, 567 (1964). DOI: 10.1103/PhysRevLett.13.567
- [6] E.A. Manykin, V.V. Samartsev. *Opticheskaya ekho-spektroskopiya* (Nauka, Moskva, 1984).
- [7] N.M. Pomerantsev. *UFN* **65**, 87 (1958) (in Russian). DOI: 10.3367/UFN.0065.195805c.0087

- [8] A.N. Oraevsky. UFN **91**, 181 (1967) (in Russian). DOI: 10.3367/UFNr.0091.196702a.0181
- [9] A.I. Alekseyev. Zh. Eksp. Teor. Fiz. Pis'ma Red, **9** (8), 285 (1969)
- [10] A.V. Evseev, I.V. Evseev, V.M. Ermachenko. Opt. i spectr., **50**, 77 (1981) (in Russian).
- [11] I.V. Evseev, V.M. Ermachenko. Opt. i spectr., **47** (1139), (In Russian)
- [12] I.V. Evseev, V.A. Reshetov. Opt. i spectr., **57**, 869, (1984) (in Russian).
- [13] N.N. Rubtsova, V.N. Ishchenko, E.B. Khvorostov, S.A. Kochubei, V.A. Reshetov, I.V. Yevseyev. Phys. Rev. A, **70**, 023403 (2004). DOI: 10.1103/PhysRevA.70.023403
- [14] T. Baer, I.D. Abella. Physical Review A, **16**, 2093 (1977). DOI: 10.1103/PhysRevA.16.2093
- [15] I.I. Popov, I.S. Bibikov, I.V. Evseev, V.V. Samartsev. Zhurnal prikladnoy spektroskopii **52**, 794 (1990) (in Russian).
- [16] V.N. Ishchenko, S.A. Kochubei, N.N. Rubtsova, E.B. Khvorostov, I.V. Yevseyev. Laser Physics, **12** (8), 1079 (2002).
- [17] R. Beach, B. Brody, S.R. Hartmann. Phys. Rev. A, **27**, 2925 (1983). DOI: 10.1103/PhysRevA.27.2925
- [18] I.V. Yevseyev, V.N. Ishchenko, S.A. Kochubei, V.A. Reshetov, N.N. Rubtsova, E.B. Khvorostov. Laser Physics, **16** (4), 535 (2006). DOI: 10.1134/S1054660X06040013
- [19] N.N. Rubtsova, V.N. Ishchenko, E.B. Khvorostov, S.A. Kochubei, I.V. Yevseyev. Laser Physics Letters, **2** (6), 309 (2005). DOI: 10.1002/lapl.200510003
- [20] M.L. Burshtein, Ya.F. Verolainen, V.A. Komarovskiy, A.L. Osheerovitch, N.P. Penkin. Opt. i spectr., **37**, 617, (1974) (in Russian).
- [21] M. Baumann, G. Wandel. Physics Letters, **22** (3), 283 (1966). DOI: 10.1016/0031-9163(66)90614-7
- [22] N.N. Rubtsova, S.A. Kochubey, E.B. Khvorostov, V.A. Reshetov. UFN **193**, 1071 (2023) (in Russian). DOI: 10.3367/UFNr.2022.11.039263
- [23] N.N. Rubtsova, V.G. Gol'dort, E.B. Khvorostov, S.A. Kochubei, V.A. Reshetov. Laser Physics, **28** (6), 066001 (2018). DOI: 10.1088/1555-6611/aabc98

*Translated by E.Ilinskaya*